Physical study of radiation effects on the boundary layer structure in a turbulent channel flow

Yufang Zhang, Ronan Vicquelin, Olivier Gicquel, J Taine

Physical study of radiation effects on the boundary layer structure in a turbulent channel flow

Y. F. Zhang[a,b], R. Vicquelin[a,b,*], O. Gicquel[a,b], J. Taine[a,b]

[a] *CNRS, UPR 288 Laboratoire d'Énergétique Moléculaire et Macroscopique, Combustion (EM2C), Grande Voie des Vignes, 92295 Châtenay-Malabry, France.*
[b] *Ecole Centrale Paris, Grande Voie des Vignes, 92295 Châtenay-Malabry, France.*

Abstract

A complete numerical coupling between radiation and turbulent convection in a channel gas flow has been performed for different temperature, optical thickness (pressure) and wall emissivity conditions. In this model, radiation is treated from the CK approach and a Monte Carlo transfer method; The flow by a Direct Numerical Simulation. Both the effects of turbulence on radiation fields and of radiation on turbulent fields are accounted for.

Gas-gas and gas-wall radiation interactions generate antagonist effects on the temperature and flux fields. The first one tends to increase wall conductive flux while the second one to decrease it. Consequently, the structure of the temperature field and the wall conductive flux often strongly differ from results without radiation. Classical wall log-laws for temperature are then strongly modified by the global radiation effects. Many conditions encountered in applications are discussed in the paper. The observed modifications depend on all the set of conditions (temperature level, wall emissivity, pressure, Reynolds number), i.e. on the relative magnitudes of radiation gas-gas and gas-wall phenomena and of global radiation flux and conductive flux without radiation.

Keywords: DNS, turbulence, gas radiation, Monte-Carlo, channel flow, temperature, wall-law

*Corresponding author. Tel.: +33 1 41 13 10 90; Fax: +33 1 47 02 80 35.
Email address: ronan.vicquelin@ecp.fr (R. Vicquelin)

Roman Symbols

c_p	Thermal capacity at constant pressure [$\mathrm{J{\cdot}kg^{-1}{\cdot}K^{-1}}$].
h	Enthalpy per unit mass [$\mathrm{J{\cdot}kg^{-1}}$].
L	Length [m].
p	Pressure [Pa].
Pr	Prandtl number [-].
P	Power per unit volume [$\mathrm{W{\cdot}m^{-3}}$].
q	Heat flux [$\mathrm{W{\cdot}m^{-2}}$].
Re	Reynolds number [-].
S_i	Momentum source term [$\mathrm{N{\cdot}m^{-3}}$].
t	Time [s].
T	Temperature [K].
u	Streamwise velocity component [$\mathrm{m{\cdot}s^{-1}}$].
u_i, u_j	Velocity vector [$\mathrm{m{\cdot}s^{-1}}$].
X, Y, Z	Cartesian coordinates [m].
x_i	Coordinate vector (tensorial) [m].
y	Distance to a wall [m].

Greek Symbols

δ	Channel half-width [m].
δ_{ij}	Kronecker delta operator [-].
κ	Spectral absorption coefficient [$\mathrm{m^{-1}}$].
λ	Thermal conductivity [$\mathrm{W{\cdot}K^{-1}{\cdot}m^{-1}}$].
μ	Dynamic viscosity [$\mathrm{kg{\cdot}s^{-1}{\cdot}m^{-1}}$].
ν	Radiation wave number [$\mathrm{cm^{-1}}$].
ρ	Gas mass density [$\mathrm{kg{\cdot}m^{-3}}$].
τ_{ij}	Viscous shear stress tensor [$\mathrm{N{\cdot}m^{-2}}$].
Ω	Solid angle [sr].

Superscript

$\sim$	Statistical estimation or Favre mean quantities.
$^-$	Reynolds mean quantities.
$''$	Favre mean fluctuating quantities.
$^+$	Wall scaled quantities.
^{exch}	Exchanged quantities.

Subscript

$_c$, $_h$	Refer to the cold wall, respectively to the hot wall.
$_b$	Bulk quantities.
$_{cd}$	Conductive quantity.
$_R$	Radiative quantity.
$_w$	Wall quantity.
$_\tau$	Friction quantity.
$_\nu$	Spectral quantity.

Abbrevation

DNS	Direct Numerical Simulation.
LES	Large Eddy Simulation.
RANS	Reynolds-Averaged Navier–Stokes equations.
ERM	Emission Reciprocity Method.
OERM	Optimized Emission Reciprocity Method.
TRI	Turbulence-Radiation Interaction

1. Introduction

In many industrial systems such as those dealing with combustion, conductive heat fluxes and radiative energy fluxes at walls condition the design stage and the material choice. Predicting these different fluxes with numerical simulations is therefore a great challenge that has been investigated in many works. From the fundamental understanding of boundary layers and radiation energy transfer, models have been proposed to calculate this quantities. Although improving the prediction of heat fluxes remains an active area in each field, the determination of radiative fluxes and conductive fluxes at walls is always done separately without considering any coupling between these two modes of energy transfer. In this paper, the coupling of radiation and turbulent forced convection is studied to investigate whether the wall heat flux and the boundary layer structure can be modified by radiative energy transfer.

The importance of Turbulence-Radiation Interaction (TRI) has been highlighted in several works. Experimental studies [1–3], theoretical analysis [4–6] and numerical simulations [7–10] have been carried out to investigate the effect of TRI in different systems and a comprehensive review is available in [11, 12]. TRI is a consequence of the highly non-linear coupling between

the radiative intensity and the turbulent temperature and gas species composition fields. It consists of two parts, namely the influence of turbulence on radiation and vice-versa. Regarding the former, turbulence leads to an increase in the medium transmissivity [1, 13], the radiative power [14, 15] and radiative heat loss [15, 16]. In order to isolate and quantify individual contributions to TRI in a statistically one-dimensional premixed combustion system, Wu et al.[7] have performed a direct numerical simulation (DNS) coupled with a Monte-Carlo method. The results reveal that the temperature self-correlation contribution is only dominant in the case with smallest optical thickness in their study. Among the three correlation terms of the absorption coefficient, the ones with the Planck function and with the incident radiative intensity are not negligible, even in the most optically thin case, while for a case with intermediate value of optical thickness, the three correlations were all significant. Deshmukh et al. [8, 9] have also studied different contributions to TRI with DNS in a statistically homogeneous isotropic non-premixed combustion system and a one-dimensional turbulent non-premixed flame. Only the latter one was fully coupled with radiation.

Regarding the effect of radiation on the flow, radiation interacts and modifies the temperature field in non-reactive flows [6, 17, 18] and in reactive flows [10, 19]. In combustion applications, the change of maximum temperature has a significant effect on NO_x emission [20]. Influence of radiation is not restricted to the average temperature field: The intensity of the temperature fluctuations changes when radiation is taken into account[19, 21]; Goncalves et al [10] have shown an impact of radiation on turbulent flame dynamics; Ghosh et al. [18] have studied the effects of radiation in a turbulent compressible channel flow and have shown that radiation modified the Reynolds stresses in the near wall layer even for an optically thin medium. Using a low-Reynolds RANS model, Soufiani et al [6] have also carried out a channel flow simulation where the wall conductive heat flux has been found to be significantly affected by radiation while, in a similar case with DNS here, Amaya et al [22] have found the effect of radiation in the boundary layer to be weak. Using a grey gas model and varying the medium optical thickness, Gupta et al [17] have shown that the temperature profile in a turbulent channel flow can be modified by radiation.

Previous studies on the impact of radiation in a channel flow configuration [6, 17, 18, 22, 23] do not expose a general trend or understanding of the influence of radiation in turbulent boundary layers. In LES and RANS, wall models are necessary to predict wall heat flux in turbulent boundary layers.

Among these models, standard wall laws are still widely used although they are only valid for relatively simple flows with zero-pressure gradient and constant fluid properties. In real applications with more complex conditions, standard wall laws might have a great inaccuracy. In order to extend their usage to practical systems, other physical effects need to be considered such as compressibility [24–26], Prandtl number effect [27, 28], streamwise pressure gradient [29, 30] or chemical reaction [31].

The objective of this paper is to study the radiation effects on the temperature field in turbulent boundary layers by considering a turbulent channel flow. DNS is performed for the flow field in order to generate high-fidelity data. For radiation simulation, a reciprocal Monte Carlo method is employed. This method is generally regarded as the most accurate one and is widely used in many applications involving radiative transfer [7, 11, 15, 32]. The two solvers are fully coupled when radiation is taken into account. The gas radiative properties are determined by means of the correlated k-distribution (CK) model or its weak absorption limit [33], depending on the pressure condition. A detailed analysis of gas-gas and gas-wall radiation effect is carried out in this paper. For the gas-gas radiation, only the energy exchange between a gas cell and the surrounding gas is accounted for, while gas-wall radiation includes only radiative energy transfer between a gas cell and the walls. A priori these two parts have different effects on the gas temperature profile and, hence, the wall heat flux.

The numerical models and approaches are presented in Section 2. In Section 3, the effects of gas-gas and gas-wall radiation are studied for both large and intermediate optical thickness medium. Results associated with different wall emissivity, wall temperature and Reynolds number are discussed in Section 4.

2. Models and numerical approaches

2.1. Flow simulation

Under the low-Mach number approximation, the mass, momentum, energy balance equations and the ideal gas equation of state write respectively, in tensorial notations

$$\frac{\partial \rho}{\partial t} + \frac{\partial (\rho u_i)}{\partial x_i} = 0, \tag{1}$$

$$\frac{\partial (\rho u_i)}{\partial t} + \frac{\partial (\rho u_i u_j)}{\partial x_j} = -\frac{\partial p}{\partial x_i} + \frac{\partial \tau_{ij}}{\partial x_j} + S_i, \tag{2}$$

$$\frac{\partial(\rho \mathrm{h})}{\partial t} + \frac{\partial(\rho u_j \mathrm{h})}{\partial x_j} = \frac{\partial p}{\partial t} - \frac{\partial q_j^{cd}}{\partial x_j} + P^R \tag{3}$$

$$p = \rho\, r\, T, \tag{4}$$

where ρ, p and u_i are the fluid mass density, pressure and velocity components, respectively. The enthalpy per unit mass h is expressed: $\mathrm{h} = \Delta h_0 + \int_{T_0}^{T} c_p(T')\, dT'$, where c_p is the mixture thermal capacity at constant pressure, T the temperature, T_0 a reference temperature and Δh_0 the corresponding standard formation enthalpy. The viscous shear stress tensor τ_{ij} and the conductive flux vector q_i^{cd} write

$$\tau_{ij} = \mu \left(\frac{\partial u_i}{\partial x_j} + \frac{\partial u_j}{\partial u_i} \right) - \frac{2\mu}{3} \left(\frac{\partial u_k}{\partial x_k} \delta_{ij} \right), \tag{5}$$

$$q_i^{cd} = -\lambda \frac{\partial T}{\partial x_i}, \tag{6}$$

where μ is the dynamic viscosity and λ the thermal conductivity. S_i is a forcing source term required in the following channel flow computations. It is uniform and is not null only in the streamwise direction. It plays the same role as the pressure gradient to drive the flow against viscous forces. P^R is the radiative power per unit volume.

A finite-volume method for massively parallel computations on complex grids, suitable for variable density flow (code YALES2 [34, 35]) is used to solve equations 1-4 with associated boundary conditions. The code is a low Mach-number solver: the pressure p is split into a uniform thermodynamic pressure p_0 and a hydrodynamic one p_1. p_0 is used in the equation of state to compute the gas density ρ, while p_1 is obtained by solving a Poisson equation to enforce mass conservation. Spatial gradients are calculated with a centered fourth order accurate scheme. Advancement in time is done with a fourth-order Runge Kutta scheme for velocity. For scalars (here enthalpy), the latter temporal scheme is blended with another fourth-order two-step scheme based on Taylor expansion [36] that is more dissipative. The blending factor is set as small as possible and yet high enough to avoid spurious oscillations in the scalar field with centered schemes. In this study, a typical value of 0.05 is retained.

2.2. Non-dimensional quantities in channel flows

For the channel flow defined in Fig. 1, bulk, practical and friction Reynolds numbers Re_b, Re_{D_h} and Re_τ are respectively defined by

$$\mathrm{Re}_b = \frac{\rho_b\, u_b\, \delta}{\mu_b}, \quad \mathrm{Re}_{D_h} = 4\mathrm{Re}_b, \quad \mathrm{Re}_\tau = \frac{\overline{\rho_w}\, u_\tau\, \delta}{\overline{\mu_w}} \tag{7}$$

$$\text{with} \quad \rho_b = \frac{\int_0^{2\delta} \overline{\rho} dY}{2\delta}, \quad u_b = \frac{\int_0^{2\delta} \overline{\rho u} dY}{\int_0^{2\delta} \overline{\rho} dY}, \quad \mu_b = \mu(T_b)\,; \tag{8}$$

The bulk enthalpy per mass unit and the friction velocity, based on the wall viscous stress $\overline{\tau_w}$, by

$$\mathrm{h}_b = \frac{\int_0^{2\delta} \overline{\rho u \mathrm{h}} dY}{\int_0^{2\delta} \overline{\rho u} dY}, \quad u_\tau = \left(\frac{\overline{\tau_w}}{\overline{\rho_w}}\right)^{1/2}, \tag{9}$$

where indices b and w are related to bulk and wall quantities, respectively, and $\overline{\cdot}$ refers to average quantities. The bulk temperature T_b is evaluated from the bulk enthalpy : $\mathrm{h}_b = \mathrm{h}(T_b)$. When the channel flow case is not symmetrical ($T_{w,c} \neq T_{w,h}$), the friction velocity is different on both walls: $u_{\tau,c} \neq u_{\tau,h}$ and, therefore: $\mathrm{Re}_{\tau,c} \neq \mathrm{Re}_{\tau,h}$.

The non-dimensional distance y^+, based on the distance to a wall y, the non-dimensional streamwise velocity $\overline{u}^+$, and the non-dimensional temperature $\overline{T}^+$ are written

$$y^+ = \frac{\overline{\rho_w}\, y\, u_\tau}{\overline{\mu_w}}, \quad \overline{u}^+ = \frac{\overline{u}}{u_\tau}, \quad \overline{T}^+ = \frac{|\overline{T} - T_w|}{T_\tau}, \tag{10}$$

where T_τ is the friction temperature defined by

$$T_\tau = \frac{|\overline{q_w^{cd}}|}{\overline{\rho_w}\ \overline{c_{p_w}}\, u_\tau}, \tag{11}$$

where q_w^{cd} is the wall conductive flux, chosen positive in the Y direction. According to this definition and Fig. 1, q_w^{cd} is negative on both walls since $T_{w,c} \leq T_{w,h}$.

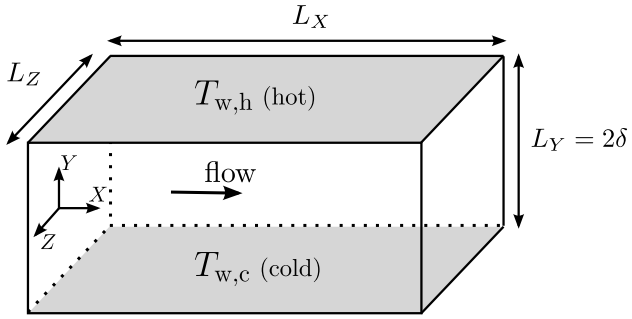

Figure 1: Computational domain of channel flow cases. X, Y and Z are the streamwise, wall normal and spanwise directions. L_X, L_Y and L_Z are the dimensions of the channel case in each direction. δ is the channel half-width. The lower wall (resp. upper wall) is at temperature $T_{w,c}$ (resp. $T_{w,h}$; $T_{w,h} \geq T_{w,c}$). Periodic boundary conditions are applied along X and Z.

2.3. Validation of the flow simulation

In order to test the suitability of the code for direct numerical simulations, the channel flow case of Kim and Moin [37, 38] is computed and taken as reference for cases where temperature acts as a passive scalar. This case, named C0, is defined in Tab. 1. The discretization of the domain, defined in Tab. 2, is uniform along X and Z. ΔX, the cell length in the X direction, is expressed in wall units:

$$\Delta X^+ = \frac{\overline{\rho_w} \Delta X u_\tau}{\overline{\mu_w}}. \tag{12}$$

ΔY^+ and ΔZ^+, associated with the cell lengths ΔY and ΔZ in the Y and Z directions respectively, are defined similarly. The mesh is refined along the Y direction close to the wall where $\Delta Y^+ = 0.8$. The size of the domain was chosen large enough for results to be independent of this parameter.

For this case C0 only, density and gas properties are uniform and $T_{w,c} = T_{w,h}$. Three temperature fields associated with three values of Prandtl numbers $\mathrm{Pr}_1 = 0.1$, $\mathrm{Pr}_2 = 0.71$ and $\mathrm{Pr}_3 = 2.0$ are simulated. In this case, the temperature behaves like a passive scalar and non-dimensional results do not depend on the actual value of $T_{w,c}$. A uniform source term is added in the energy equation as in Ref. [38] to counterbalance conductive heat fluxes at the walls.

The non-dimensional mean velocity $\overline{u}^+$ and the scalar $\overline{T}^+$ are plotted in Fig. 2 and compared to numerical results of Kim and Moin [37, 38], and to

	$\mathrm{Re_b}$	Re_{D_h}	$T_{w,c}$(K)	$T_{w,h}$(K)	p(atm)
C0	2800	11200	—	—	1.0
C1	5850	23400	950	1150	40.0
C2					1.0
C3			950	2050	40.0
C4	11750	47000	950	1150	40.0

Table 1: Channel flow parameters. In case C0, non-dimensional passive scalars are considered. Reynolds numbers are given with an accuracy of 0.5 %.

	$n_X \times n_Y \times n_Z$	ΔX^+ hot/cold	ΔY^+	ΔZ^+ hot/cold
C0	$120 \times 100 \times 120$	17.85/17.85	[0.8—8.0]	8.92/8.92
C1,C2	$110 \times 135 \times 110$	16.9/21.3	[0.8—8.0]	8.4/10.6
C3	$160 \times 163 \times 160$	8.9/22.4	[0.8—8.0]	4.4/11.2
C4	$200 \times 230 \times 200$	17.3/21.8	[0.8—8.0]	8.6/10.8

Table 2: Discretization of the simulated cases: n_X, respectively n_Y and n_Z, is the number of points in the X direction, respectively Y and Z direction. Domain size: $(4\pi\delta, 2\delta, 2\pi\delta)$ for C0 and $(2\pi\delta, 2\delta, \pi\delta)$ for C1-C4. ΔX^+ and ΔZ^+ are given at the cold and hot sides for C1-C4.

the log-law obtained by these authors: $u^+ = 2.5\ \ln y^+ + 5.5$, in Fig. 2 a and to the log-law of Kasagi et al. [39]: $T^+ = 2.78\ \ln y^+ + 2.09$, in Fig. 2 b. Good agreement is obtained between our results and those of the previous authors, demonstrating the accuracy of the chosen numerical set up to perform DNS of channel flows.

2.4. Radiation simulation

The general organization of the radiation model, based on a reciprocal Monte Carlo approach, has been detailed by Tesse et al. [40]. This model has been previously applied to combusting media involving radiation [15] and improved in [41]. Only the principles of the method are briefly summarized here.

In the approach of Ref.[40], the radiation computational domain is discretized into N_v and N_f isothermal finite cells of volume V_i and faces of area

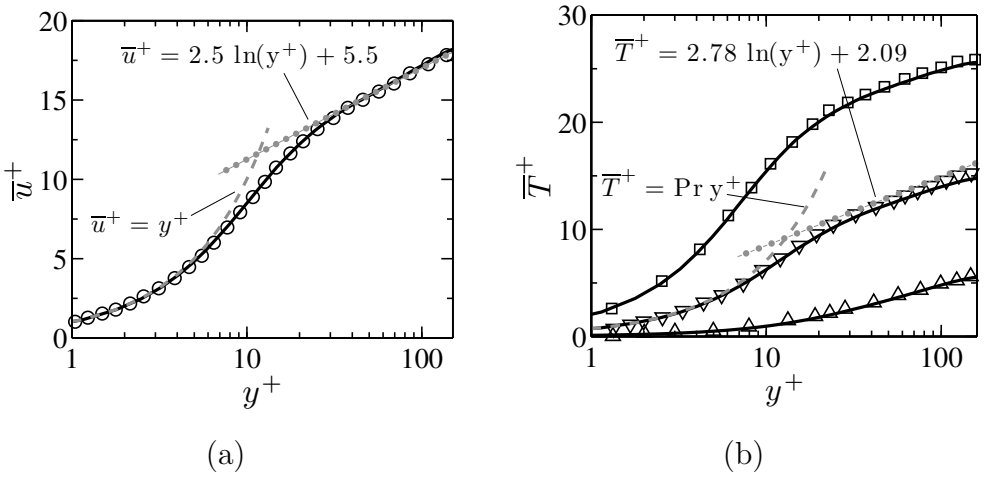

(a) (b)

Figure 2: Mean profiles of non-dimensional streamwise velocity (a): ◯ [37]; and non-dimensional temperature in wall units (b): △(Pr = 0.1), ▽(Pr = 0.71), □(Pr = 2) [38]; ▬ : present results.

S_i, respectively. The radiative power in any cell i is written as the sum of the exchange powers P_{ij}^{exch} between i and all the other cells j, *i.e.*

$$P_i = \sum_{j=1}^{N_v+N_f} P_{ij}^{exch} = -\sum_{j=1}^{N_v+N_f} P_{ji}^{exch}. \tag{13}$$

For volume cells, for instance, P_{ij}^{exch} is given by

$$P_{ij}^{exch} = \int_0^{+\infty} \kappa_\nu(T_i)[I_\nu^\circ(T_j) - I_\nu^\circ(T_i)] \int_{V_i}\int_{4\pi} A_{ij\,\nu} d\Omega_i dV_i d\nu, \tag{14}$$

where $I_\nu^\circ(T)$ is the equilibrium spectral intensity and $\kappa_\nu(T_i)$ the spectral absorption coefficient relative to the cell i. $d\Omega$ is an elementary solid angle and $A_{ij\,\nu}$ accounts for all the paths between emission from any point of the cell i and absorption in any point of the cell j, after transmission, scattering and possible wall reflections along the paths. Its expression and similar expressions for exchanges between a volume cell and a surface cell or between two surface cells are detailed in Ref.[40].

In the reciprocity Monte Carlo method, a huge number of optical shots are issued from the cells. Statistical estimation $\tilde{P}_{ij}^{exch}$ of P_{ij}^{exch} are obtained by

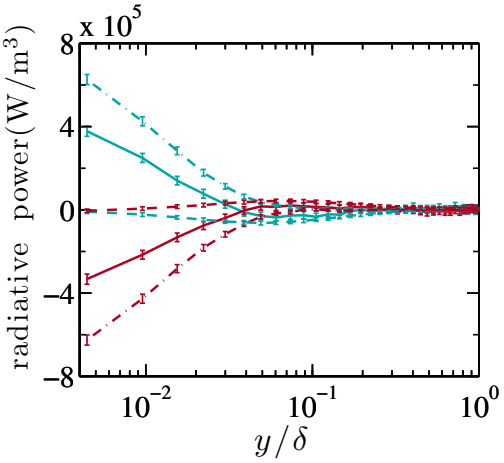

Figure 3: Comparison of mean radiative power of C1R1, C1R1_GG and C1R1_GW (—— : C1R1; – – : C1R1_GW; – · – : C1R1_GG; color —— : Cold side; color —— : Hot side; error bars represent the standard deviation).

summing the contributions of the N_{ij} shots that connect i and j, *i.e.*

$$\widetilde{P}_{ij}^{exch} = \sum_{n=1}^{N_{ij}} P_{ijn\nu}^{exch}. \tag{15}$$

In order to increase the computational efficiency, emission is here only carried out from arbitrary small spheres around grid points instead of using finite grid cells that are neither isothermal nor homogeneous. In this condition, the small emission spheres are isothermal, homogeneous and optically thin. A consequence of this choice is that the Absorption-based Reciprocity Method (ARM), which requires emission from finite cell, is not suitable. Only Emission-based Reciprocity Methods (ERM) can then be used. In order to overcome some drawbacks of ERM compared to ARM in cold regions of the medium, the Optimized Emission Based Reciprocity Method (OERM), proposed by Zhang et al. [41], is here used for the radiation frequency treatment.

An other advantage of ERM and OERM method is to allow the Monte Carlo convergence to be locally controlled. In all the present simulations a radiative power standard deviation of 3% of radiative power maximum value has been imposed at any grid point (as shown in Fig. 3 for instance).

	R1	R2	R3	R4
ϵ_1 (cold wall)	0.8	0.3	0.1	0.1
ϵ_2 (hot wall)	0.8	0.3	0.1	1.0

Table 3: Wall emissivities in radiative conditions R1, R2, R3 and R4.

2.5. Coupled simulation

For all cases considered in the paper, a non-reacting CO_2-H_2O-N_2 gas mixture flows, in developed turbulent regime, through a plane channel in different conditions. The molar fractions of CO_2, H_2O and N_2 are 0.116, 0.155 and 0.729. Cases involving radiation cannot be entirely characterized by non-dimensional numbers, contrary to cases without radiation. The value of δ, the channel half-width, is then given here: $\delta = 0.1$ m.

The dynamic viscosity μ is computed as a function of temperature from the CHEMKIN package [42, 43] for the chosen mixture composition. The thermal conductivity λ is computed from a Prandtl number Pr. In all considered configurations, the Prandtl number is very close to the chosen value 0.71.

The flow computational cases, called Cn (n= 1 to 4), are defined in Table 1 by a set of bulk Reynolds number Re_b, pressure and wall temperatures. Similarly, cases which include radiative energy transfer are called Rm (m= 1 to 4) and are defined by the emissivities (ε_1, ε_2) of the opaque walls given in Table 3. Consequently, a computation case without radiation in conditions n is called Cn and a computation that accounts for radiation effects, in conditions n and m, CnRm. The associated spatial discretizations are defined in Table 2.

Gas radiative properties are treated in a correlated manner by the CK approach for atmospheric pressure condition, and by using the weak absorption limit for high pressure cases [33]. In the directions X and Z, periodicity conditions are also used for radiation simulation, *i.e.*, if a shot exits the domain, for instance, at the point (L_X, Y, Z), it will enter at the point $(0, Y, Z)$ with the same propagation direction. The grid of the radiation model is three times coarser in X direction and two times in Y and Z directions than the corresponding grid of the flow model.
In the chosen DNS conditions, all averaged fluxes are uniform in directions

X and Z. The averaged energy balance equation then writes, from Eq. 3,

$$\frac{d}{dY}\left[\overline{\rho}\widetilde{v''\mathrm{h}''}(Y) + \overline{q^{cd}}(Y) + \overline{q^{R}}(Y)\right] = \frac{d}{dY}\,\overline{q^{tot}} = 0, \tag{16}$$

where $\overline{\rho}\widetilde{v''\mathrm{h}''}$, $\overline{q^{cd}}$, and $\overline{q^{R}}$ and $\overline{q^{tot}}$ are the averaged turbulent convective heat flux, conductive flux, radiative energy flux and total flux, respectively. This total flux is also uniform along Y. Note that, the radiative energy flux can be split into two parts :

$$\overline{q^{R}}(Y) = \overline{q^{R*}}(Y) + \overline{q^{R}_{ww}}, \tag{17}$$

where $\overline{q^{R}_{ww}}$ is the flux exchanged between the walls through the whole gaseous medium, that does not participate to the fluid energy balance and is zero if the walls are at the same temperature, as encountered in many applications. In the studied configurations, it is always uniform. Then Equation 16 writes

$$\overline{\rho}\widetilde{v''\mathrm{h}''}(Y) + \overline{q^{cd}}(Y) + \overline{q^{R*}}(Y) = \overline{q_w}\,, \tag{18}$$

where $\overline{q_w} = \overline{q^{tot}}$ is the total flux exchanged between a wall and the gaseous mixture without the wall-wall radiation contribution. At the wall $Y = \delta$, for instance, $\overline{q_w}$ writes

$$\overline{q_w} = \overline{q^{cd}}(Y = \delta) + \overline{q^{R*}}(Y = \delta) = \overline{q^{cd}_w} + \overline{q^{R*}_w}. \tag{19}$$

The balance of these three terms in Eq. 18 is presented in Fig. 4 for the case C2 without radiation and the related case C2R3 which accounts for radiative energy transfer. This illustrates that radiation modifies the balance of the terms in Eq. 19 and hence, the wall conductive flux, given in Tab. 4. These complex coupling effects are progressively detailed in the next sections.

3. Effects of Gas-Gas and Gas-Wall radiative interactions

The effects of radiation are due to different coupled phenomena, in particular Gas-Gas (GG) and Gas-Wall (GW) interactions, but also possible multiple reflections. In this section, the effects of gas-gas and gas-wall interactions are separately considered. In gas-gas interaction, a given gas volume only exchanges radiative energy with all other gas volumes, while the walls only partially reflect radiation. Emission by the walls is not accounted for in the GG calculations. On the contrary, in gas-wall interaction, a given gas

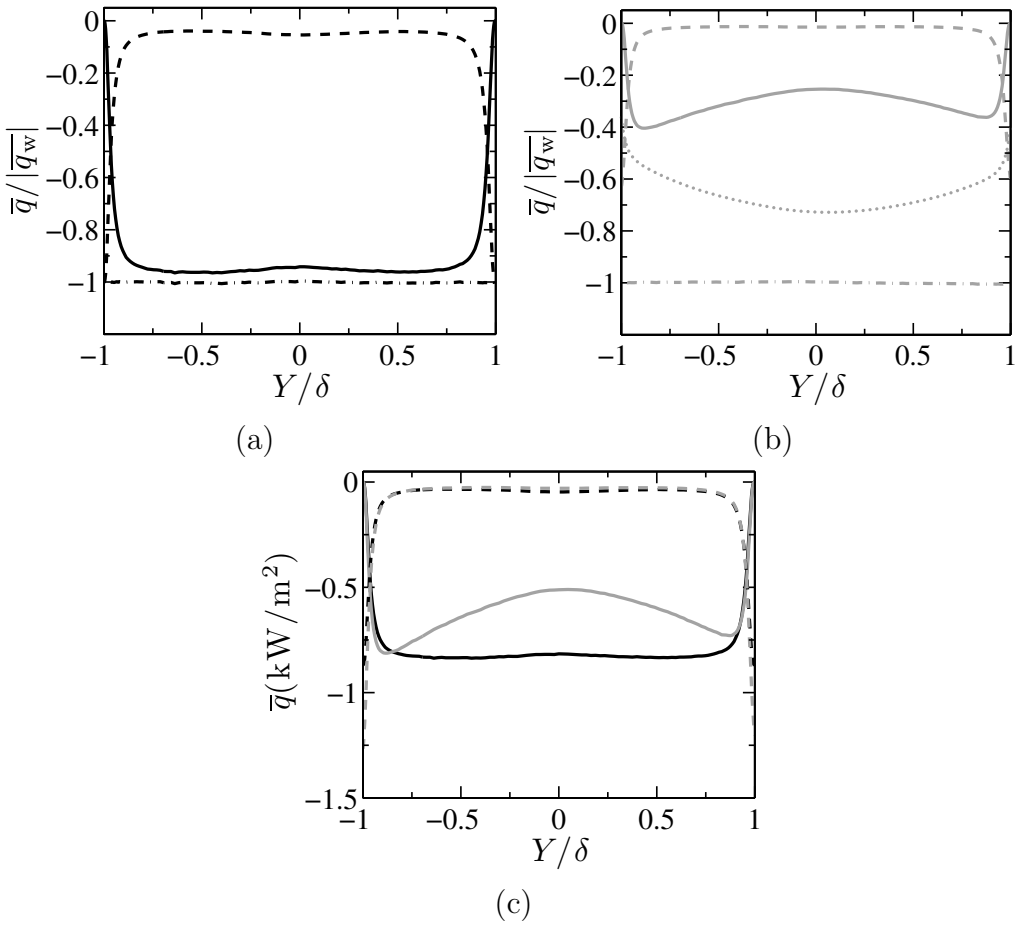

Figure 4: Mean heat flux distribution for C2 (a), C2R3 (b) and comparison of these two cases (c) (——: Turbulent convective heat flux; – –: Conductive heat flux; · · ·: Radiative energy flux; –· –: total heat flux; black lines: C2; gray lines: C2R3).

volume only exchanges energy with walls, while the other gas volumes only transmit energy. Emission by the other gas volumes is not accounted for in GW calculations. A coupled computational case that is limited to gas-gas (respectively gas-wall) radiative interactions is called CnRm_GG (respectively CnRm_GW). The obtained results are then compared with the corresponding cases CnRm, which includes all the radiation interactions, and Cn, which does not take into account radiative energy transfer.

3.1. Large optical thickness medium

In the case C1R1, defined in Tables 1 to 3 and characterized by a high pressure, the optical thickness of the gaseous mixture is large: The global medium Hotell's transmissivity at 1000 K is equal to 0.271. This allows the effects of gas-gas and gas-wall radiative interactions to be studied with a weak radiative coupling between the two walls.

Due to the small wall temperature difference, the variation in mass density in cases C1 and C1R1 is small. The profiles of the mean non-dimensional streamwise velocity $\overline{u}^+$, not shown here, are not different from the one of case C0.

The profiles of the mean temperature $\overline{T}$ associated with the cases C1 and C1R1 are compared in Fig. 5 a. The corresponding $\overline{T}^+$ profiles, for both the cold and the hot sides, are plotted in Fig. 5 b. In the case C1, without radiation, the distribution of $\overline{T}$ is practically antisymmetric and the $\overline{T}^+$ profiles are identical for the two sides. These results agree well with the results of Kim and Moin [38], obtained under the assumptions that the temperature is a passive scalar.

When only gas-wall radiation is considered, in the C1R1_GW case, the temperature gradient is smaller in the vicinity of a wall than in C1 case: The associated wall conductive fluxes presented in Table 4 are two to three times smaller than in C1 case. Indeed, the wall tends to impose its temperature to the fluid. Consequently, the temperature variation is higher in the core of the flow than in case C1. The conductive flux variations are more important at the hot side than at the cold one, as gas-wall radiative interactions strongly increase with the temperature.

On the other hand, in the case C1R1_GG, the gas-gas radiative transfer is a supplementary transfer that homogenizes the temperature field within the gas by comparison with the case C1, without radiation, as shown in Figs. 5 a and b . Consequently the temperature gradients and the conductive fluxes strongly increase at the two walls, as shown in Table 4.

	$Re_{\tau,c}$ (cold)	$Re_{\tau,h}$ (hot)	$\overline{q_{w,c}^{\mathrm{cd}}}$ (cold)	$\overline{q_{w,h}^{\mathrm{cd}}}$ (hot)	$\overline{q_{w,c}^{\mathrm{R}^*}}$ (cold)	$\overline{q_{w,h}^{\mathrm{R}^*}}$ (hot)
C0	178.5	178.5	–	–	–	–
C1	386.6	305.7	-875	-875	–	–
C1R1	390.8	303.3	-1230 (+40.6%)	-960 (+9.7%)	-6970	-7240
C1R1_GW	394.7	304.4	-460 (-47.4%)	-270 (-69.1%)	–	–
C1R1_GG	389.5	306.1	-1930 (+120.6%)	-1750 (+100.0%)	–	–
C2	386.4	305.2	-870	-870	–	–
C2R1_GW	386.3	307.9	-875 (+0.6 %)	-760 (-12.6%)	–	–
C2R1_GG	384.1	308.0	-1100 (+26.4%)	-1060 (+21.84%)	–	–
C2R1	386.3	307.1	-1070 (+23.0%)	-930 (+6.9%)	-2580	-2720
C2R2	386.6	306.4	-1220 (+40.2%)	-1100 (+26.4%)	-1480	-1600
C2R3	387.4	307.1	-1280 (+47.1%)	-1210 (+39.1%)	-730	-800
C2R4	401.1	324.5	-2060 (+136.8%)	-350 (-59.8%)	-460	-2170
C3	578.3	229.3	-6510	-6510	–	–
C3R1	668.2	260.5	-16260 (+149.8%)	-8720 (+34.0%)	-114560	-122100
C4	719.7	557.1	-1550	-1550	–	–
C4R1	723.3	566.9	-1650 (+6.5%)	-1290 (-16.8%)	-7210	-7570

Table 4: Wall fluxes (in W/m^2) $\overline{q_w^{\mathrm{cd}}}$ and $\overline{q_w^{\mathrm{R}^*}}$ for different cases at cold and hot walls (see Eqs. 16 and 17). For each case CnRm, the relative variation of $\overline{q_w^{\mathrm{cd}}}$ compared to the case Cn without radiation is put between parentheses. Flux values are rounded, typical errors are within 2-3 %.

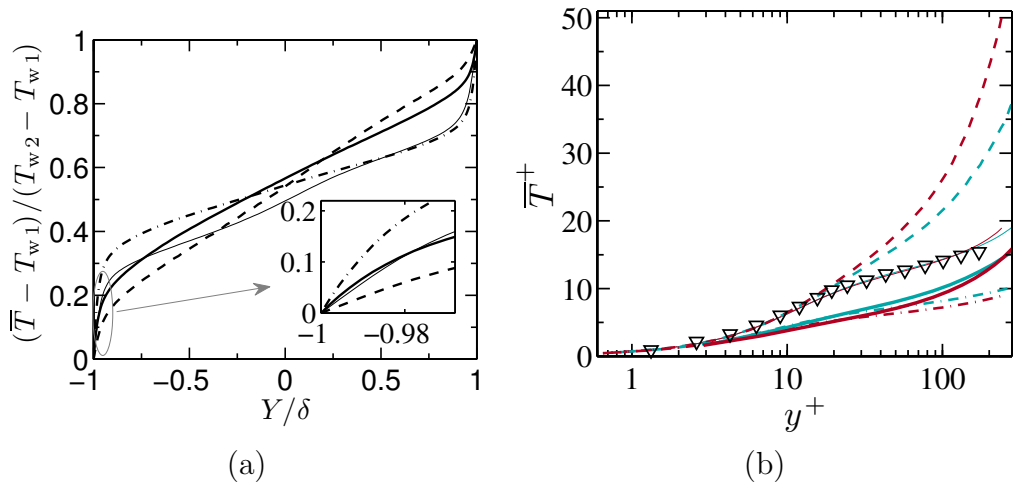

Figure 5: Mean temperature profiles in global coordinates (a) and in wall units (b): ▽ DNS results (Pr= 0.71) [38]; —— : C1; – – : C1R1_GW; – · – : C1R1_GG; —— : C1R1; in (b), —— : Cold side; color —— : Hot side.

When all the radiative effects are accounted for, in the case C1R1, the gas-gas and gas-wall interactions, that have opposite effects, are coupled. As shown in Fig. 3, in the vicinity of the wall, the amplitude of the radiative power associated with gas-gas interaction is much larger than the one associated with gas-wall interactions. Consequently, in the present conditions, the wall temperature gradients and the conductive fluxes increase, as in the gas-gas case, at the two walls by comparison with the case C1 without radiation, as shown in Tab. 4 and Fig. 5 a.

An important result is that, in this case, no log-law can be clearly identified.

3.2. Intermediate optical thickness medium

All the previous study has been again carried out for the case C2R1, characterized by a fluid at atmospheric pressure instead of 40 atm, but with the same data as for C1R1 (Re_b, δ, T_1, T_2, ε_1, ε_2). In these new conditions, the optical thickness of the medium is much smaller than previously. The global Hotell's transmissivity at 1000 K of the channel is equal to 0.811. Consequently, interaction phenomena between the two walls now occur, due to multiple reflections. Results are shown in Figs. 6 a, b and c. The same analysis as previously can be drawn, but the effects related to gas-gas and gas-wall interactions are smaller than at high-pressure. As shown in Tab. 4 , the

conductive fluxes obtained by only accounting for gas-gas interaction (case C2R1_GG) for the two sides are larger than the conductive fluxes associated with the case C2, without radiation. On the contrary, the conductive fluxes obtained in case C2 and by only accounting for gas-wall interaction (case C2R1_GW) are close, especially at the cold side. Finally, the conductive flux associated with all radiation effects (C2R1) is larger than in the C2 case at the two walls as in the optically thick case. Moreover, the temperature fields obtained by accounting for all radiation effects differ from the fields computed without radiation. Once again the profiles associated with the case C2 agree with the temperature profile of [38] while it is not any more valid when radiation is accounted for.

As for the case C1R1, the usual thermal log-law is not valid in this case.

4. Influences of different parameters

The radiation intensity field and, consequently, the radiative power and the temperature fields within the gaseous medium are strongly influenced by the wall emissivities, the wall temperatures and the bulk Reynolds number of the flow. The roles of these three quantities are studied in this Section.

4.1. Influence of wall emissivity

Three other couples of wall emissivities are now considered, in the conditions C2 of the flow at atmospheric pressure: These radiative conditions R2, R3 and R4 are defined in Tab. 3. From a practical point of view, an emissivity of about 0.8 typically corresponds to walls made of oxides, an emissivity of about 0.3 to polished metals. Emissivities of 0.1 and 1 are extreme cases.

The mean temperature fields associated with C2, C2R1, C2R2 and C2R3 cases are plotted in Fig. 7 a. When the wall emissivity decreases, gas-gas effects become more and more important and the temperature profile becomes more uniform in the flow center part while the temperature gradient near the wall increases, as shown in Tab. 4. Similarly, $\overline{T}^+$ decreases on both sides when the wall emissivity decreases. Only the cold side results are shown in Fig. 7 b.

The antagonist gas-gas and gas-wall effects also appear on the average radiative power field shown in Fig. 8 a. On both walls, the radiative power magnitude increases when wall emissivities decrease. This global effect can be analyzed from gas-gas and gas-wall exact contributions to the total radiative power in cases C2Rm. These contributions are given in Figs. 8 b and c.

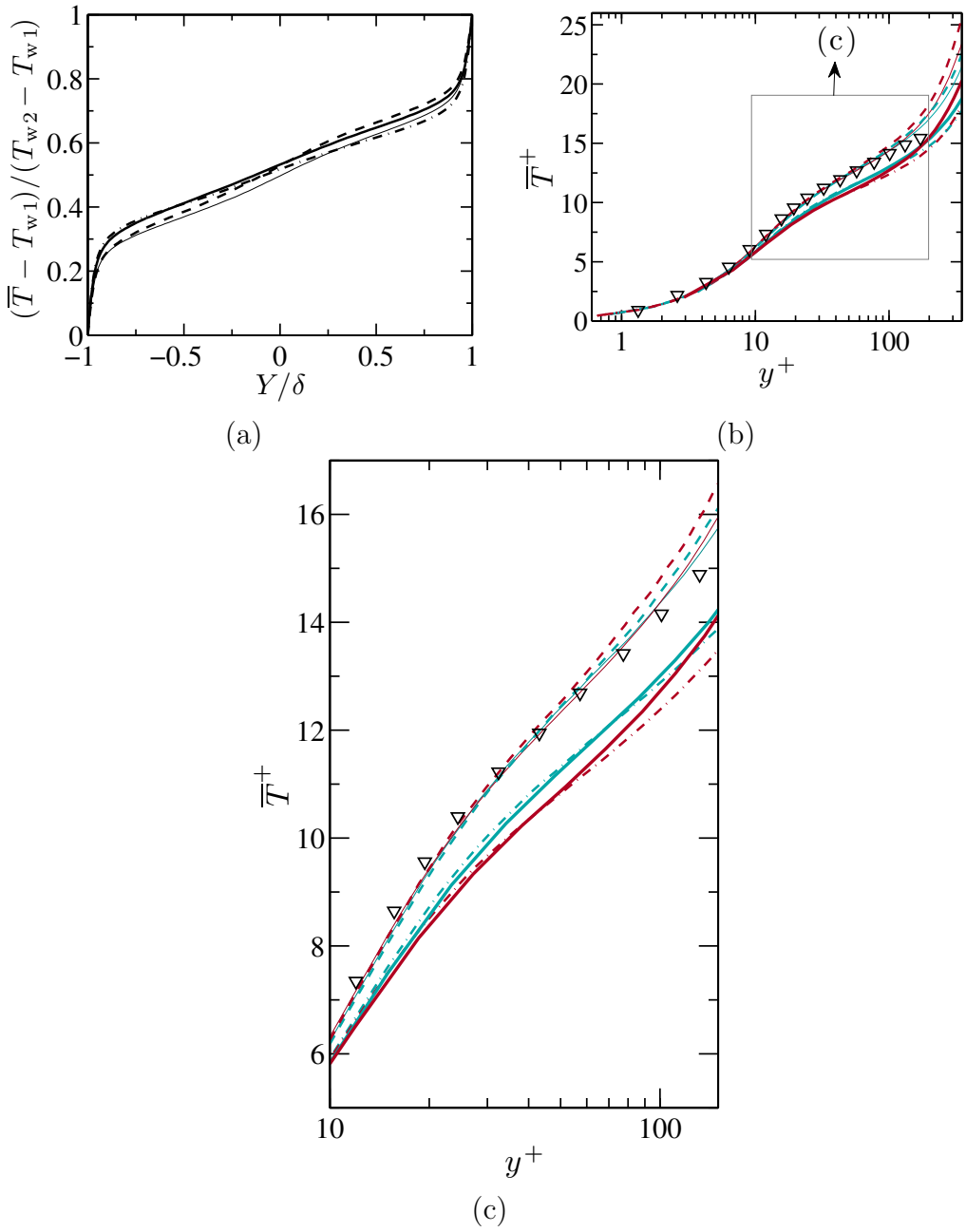

Figure 6: Comparison of mean temperature profile (a), $\overline{T}^+$ profile (b,c) of C2, C2R1_GW, C2R1_GG and C2R1 ($\triangledown$: DNS results of a passive scalar of Kim and Moin [37] (with Pr=0.71); —— : C2; – – : C2R1_GW; – · – : C2R1_GW; —— : C2R1; in (b), color —— : Cold side; color —— : Hot side).

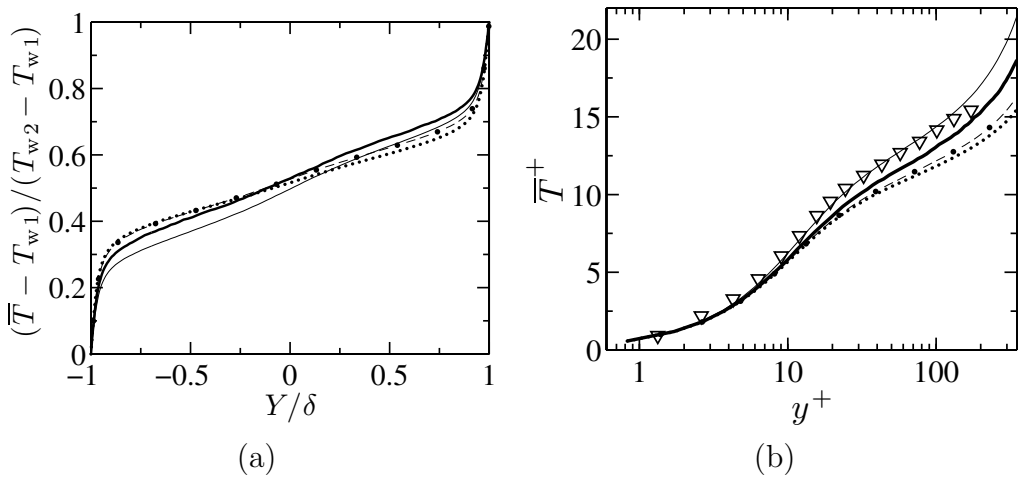

Figure 7: Mean profile of temperature (a), $\overline{T}^+$ on the cold side (b) for C2, C2R1, C2R2 and C2R3 ($\bigtriangledown$: DNS results of a passive scalar of Kim and Moin [37] (with Pr=0.71); —— : C2; —— : C2R1; – – · : C2R2; · · · : C2R3).

When wall emissivity decreases, the reflected flux and possibly the number of reflections increase. Consequently, the gas-gas interaction effects increase as seen in Fig. 8 b . On the other hand, the flux exchanged between the gas and the walls and, hence, the gas-wall interaction effects decrease as seen in Fig. 8 c. The shape of the gas-wall contribution to the total radiative power is explained by splitting the gas-wall interaction into a gas-cold-wall and a gas-hot-wall interactions. These latter contributions are given in Fig. 8 d. Finally, the global radiative power is the sum of all contributions and follows the same trend as the gas-gas interaction which is significantly larger than the gas-wall interaction in these cases.

The radiative conditions R4 (see Tab. 3) corresponds to two extreme cases: Very reflecting cold wall of emissivity 0.1 and black hot wall. The previous effects on the averaged temperature field are here amplified, as shown in Fig. 9 a, by comparing the cases C2, C2R3 and C2R4. For case C2R4, the hot black wall strongly imposes its temperature to the close gaseous layer. In the other hand, the reflecting cold wall strongly increase gas-gas radiative interactions and homogenizes the fluid temperature. The cumulation of these effects leads to: i) A much smaller temperature gradient and conductive flux at the hot wall than in case C2R3 associated with an emissivity equal to 0.1 (see Tab. 4); ii) A weak averaged temperature variation in the core of the

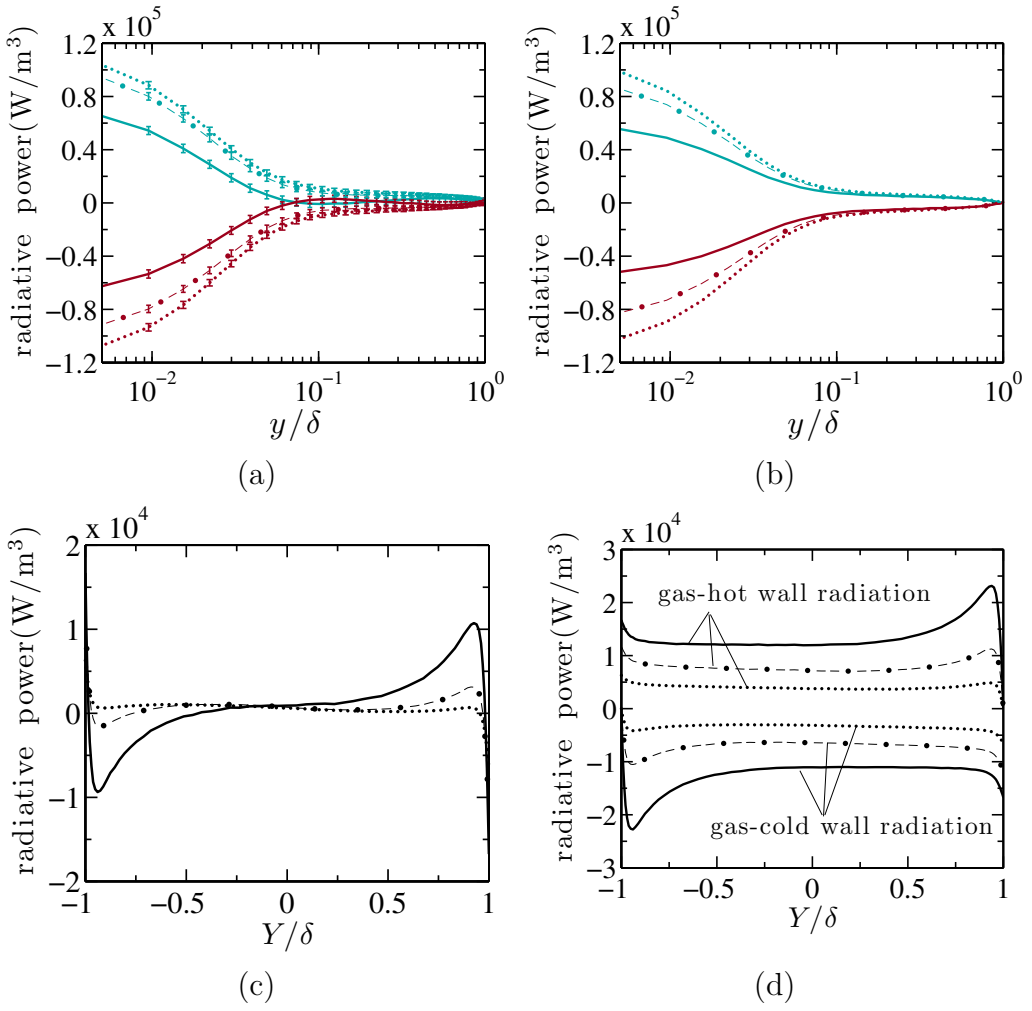

Figure 8: Mean profile of total radiative power (a), gas-gas radiative power (b), gas-wall radiative power (c) and gas-cold wall and gas-hot wall radiative power (d) of C2R1, C2R2 and C2R3 (—— : C2R1; – – · : C2R2; · · · : C2R3; in (a) and (b), color —— : Cold side; color —— : Hot side; error bars in (a) represents standard deviation).

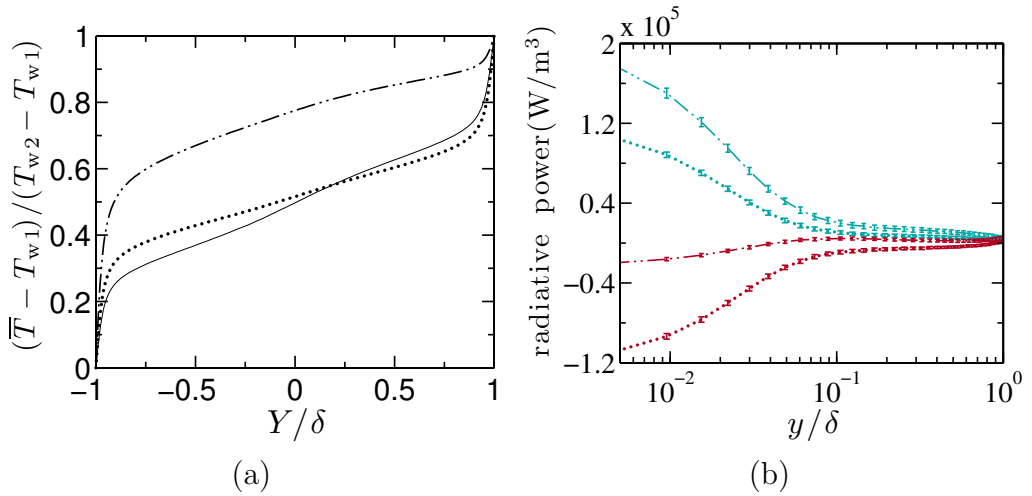

Figure 9: Mean profile of temperature of C2, C2R3 and C2R4 (a) and radiative power of C2R3 and C2R4 (b) (—— : C2; $\cdots$: C2R3; —$\cdot\cdot$— : C2R4; in (b), color —— : Cold side; color —— : Hot side; error bars in (b) represent standard deviation).

gaseous medium; iii) Consequently the temperature gradient at the cold wall and the associated conductive flux are much larger than in case C2R3, as shown in Tab. 4 .

The radiative power fields of the two extreme cases C2R3 and C2R4 differ in the vicinity of both walls as shown in Fig. 9 b. It can be explained by the previously discussed cumulative effects on the temperature profile : On the hot side, the gas temperature is close to the hot wall temperature, which decreases the magnitude of the radiative power; On the cold side, both the black hot wall and the large hot region contribute to increase the radiative power.

Figure 10 shows the radiative power field in the hot half part of the channel. It appears that the radiative power in case C2R3 is dominated by gas-gas interaction. On the contrary, in the case C2R4, gas-wall interaction overcomes gas-gas interaction except for the close vicinity of the hot wall. For intermediate emissivity value, intermediate radiative power fields are encountered.

Note that, in the present simple case as in most of the previous ones, both gas-wall and gas-gas radiative interactions are strongly modified by the wall reflection, as the optical thickness of the mediums is weak. Gas-gas an gas-wall interactions are not isolated phenomena, as in case C1Rm

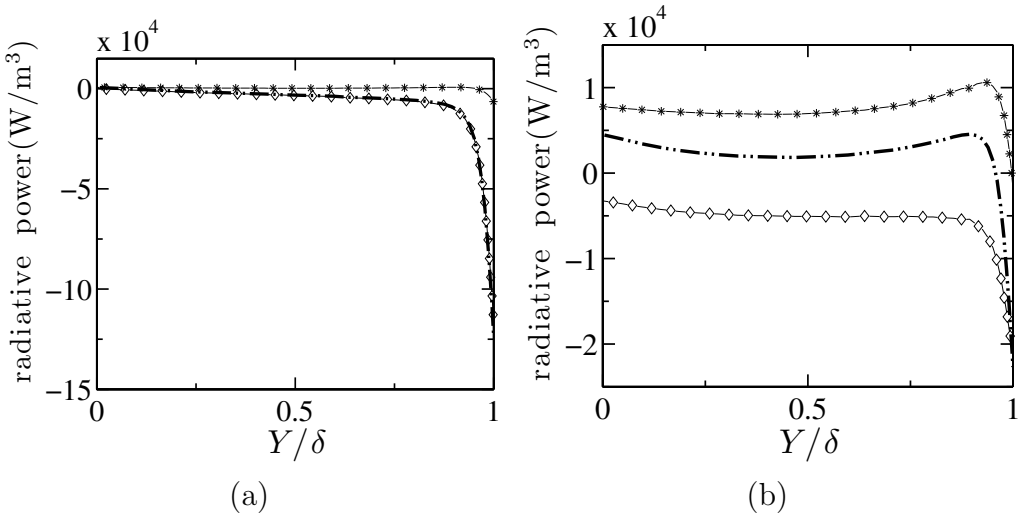

Figure 10: Mean profile of radiative power for the channel hot side for C2R3 (a) and C2R4 (b) (— ·· — : Total; —∗—: Gas-wall; —◇— : Gas-gas).

at high-pressure, characterized by a large global optical thickness. The wall reflection law and the medium optical thickness have important effects on the temperature fields as they can enhance or reduce the gas-gas or the gas-wall contributions.

4.2. Influence of the temperature

In order to study the influence of both the temperature level and the temperature difference, the C3 and C3R1 cases considered. They are characterized by wall temperatures equal to 950K and 2050K. On the cold side, these data correspond to classical combustion applications at high pressure. The associated results are compared with those of C1 and C1R1 cases.

Contrary to the previous cases, the gaseous medium density strongly varies for C3 and C3R1 cases and variations in the averaged velocity profiles are now observed in Fig. 11 a. Similarly, differences between the $\overline{u}^+$ profiles are observed in Fig. 11 b, showing that the classical velocity log-law is not valid any more. However, if the Van Driest transformation, defined by

$$\overline{u}^+_{VD} = \int_0^{\overline{u}^+} \sqrt{\frac{\overline{\rho}}{\overline{\rho}_w}} d\overline{u}^+, \tag{20}$$

is used to account for variable density effects, all velocity profiles collapse to the usual log-law (see Fig. 11 c).

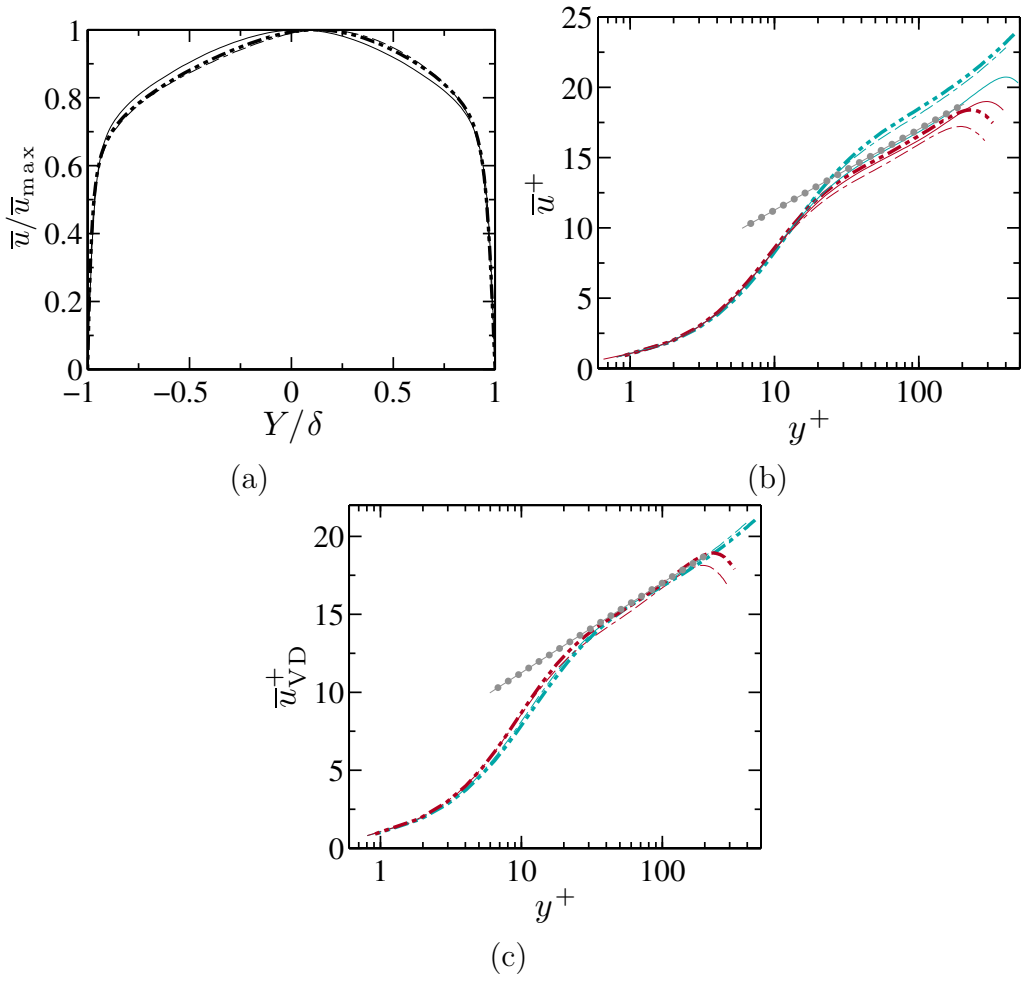

Figure 11: Mean profile of velocity (a), $\overline{u}^+$ (b) and $\overline{u}^+_{VD}$ (c) of C3, C3R1 and C1 (—●—: Wall function of Ref. [37]; – – - : C3; —··— : C3R1; —— : C1; in (b) and (c), color —— : Cold side; color —— : Hot side).

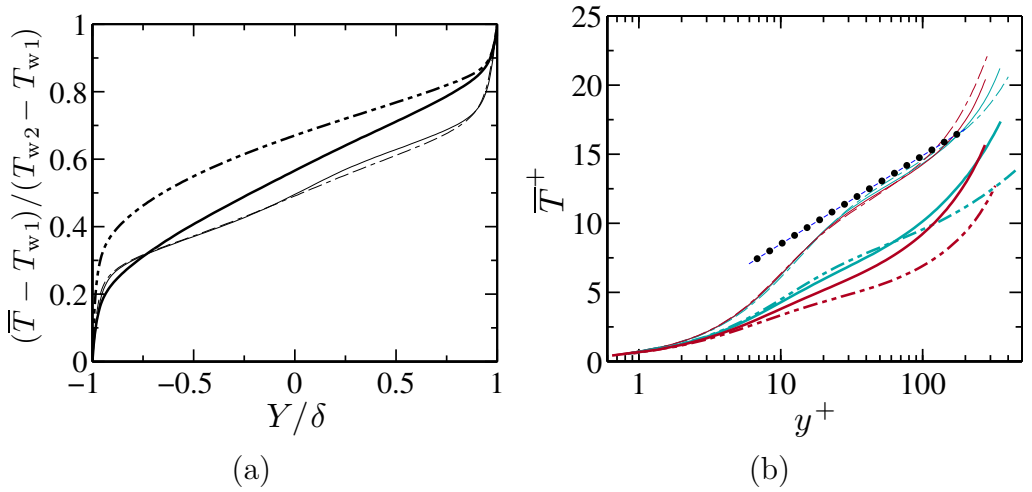

Figure 12: Mean profile of mean temperature(a) and $\overline{T}^+$(b) of C3, C3R1, C1 and C1R1 (–●– : Wall function of Ref. [39]; – – – : C3; —·· — : C3R1; —— : C1; ——: C1R1; in (b), color —— : Cold side; color —— : Hot side).

The averaged temperature profile of C3R1 case is compared in Fig. 12 a with those of C3, C1 and C1R1. As the temperature of the hot wall is much higher in C3R1 case than in C1R1 case, the radiative transfer is much stronger in this case (see $\overline{q_w^{R*}}$ in Tab. 4) and the opposite effects of gas-gas and gas-wall radiative interactions shown in this latter case are amplified. The same analysis as for the case C1R1 can be achieved (see Sec. 3.1) and the results are similar, with an amplification effect for the conductive fluxes, as given in Tab. 4. Consequently, the averaged temperature is much higher than in C3 case. Figure 12 b shows that the usual log-law is not valid when radiation is accounted for. Moreover, no temperature log-law even appears between $y^+ = 30$ and $y^+ = 200$.

4.3. Influence of the Reynolds number

The results of the C4 and C4R1 cases, characterized by a higher Reynolds number than previously (see Tab. 1), are here compared with cases C1 and C1R1 in order to study the influence of the Reynolds number. The temperature profiles are plotted in Fig. 13. The curve $\overline{T}^+(y^+)$ for case C4R1 in Fig. 13 b lies between the ones where radiation is not accounted for and the one of case C1R1. Increasing the Reynolds number between cases C1R1 and C4R1 has then moved the obtained wall-law closer to the usual one. There

are two different explanations for this behavior.

First, by increasing the Reynolds number, turbulent transport has been enhanced and its weight compared to the other energy transfer mechanisms is increased. This is shown in Fig. 14 a where turbulent transport is twice larger in case C4R1 than in case C1R1. One effect of the Reynolds number is therefore to relax the curve $\overline{T}^+(y^+)$ obtained when radiation effects are considered towards the usual law of the wall which should be retrieved when radiative energy transfer is negligible.

In addition to this first effect, there is a second one that deals with a modification of the radiative energy transfer. In this specific configuration, the gas-gas and gas-wall radiative contributions to the total radiative power field in case C4R1 are modified as shown in Fig. 15 where they are compared to results in case C1R1. Magnitude of the gas-gas contribution decreases for the larger Reynolds number case while the magnitude of the gas-wall contribution increases. Since a larger Reynolds number leads to a larger gradient of the mean temperature close to the wall, the gas temperature at a given position gets closer to the average one in the core of the channel when the Reynolds number increases, while its difference with the near wall temperature gets larger. This explains the observed trends for the gas-gas and gas-wall radiative contributions. Consequently, the gas-gas effects on the wall conductive heat flux and the wall law dwindle while the gas-wall effects grow. This is seen in Tab. 4 where the conductive heat flux increase on the cold wall due to radiation is less in case C4R1 than in case C1R1. On the hot wall, the conductive heat flux even decreases between cases C4 and C4R1, showing that gas-wall effects overcome gas-gas effects there. Finally, the modification of the gas-gas and gas-wall contributions make the observed wall law go up compared to case C1R1.

Among these two effects of the Reynolds number, the latter one is dominant in the present configuration where the radiative flux is much larger than turbulent transport (see Fig. 14). Would radiation remain dominant, increasing the Reynolds number even more could move the curve $\overline{T}^+(y^+)$ above the usual wall law. This could not be check here due to the limitations of DNS on computational ressources with increasing Reynolds numbers.

5. Conclusion

In practical conditions of coupling between turbulent convection and radiation, there is no simple way for accurately predicting the averaged tem-

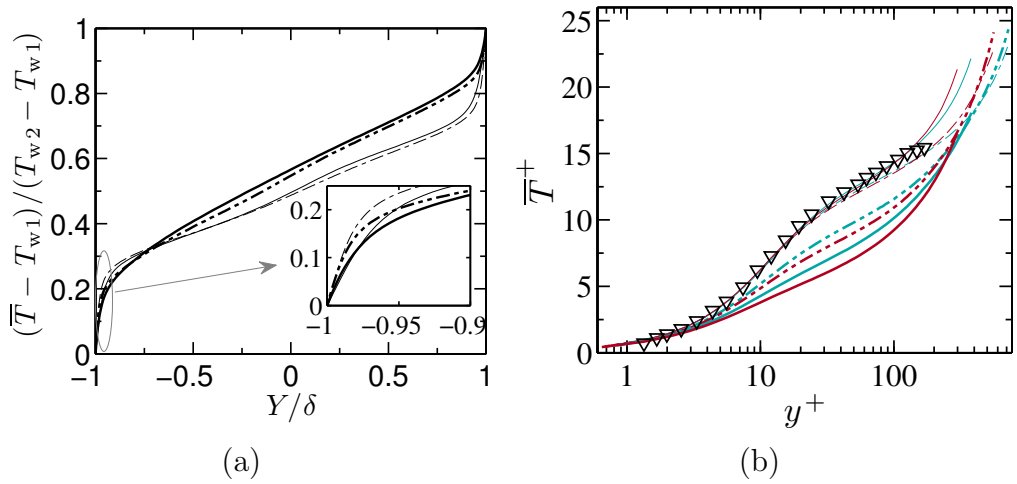

Figure 13: Mean temperature profile (a) and $\overline{T}^+$ of C4, C4R1, C1 and C1R1 (b) (– – · : C4; —··— : C4R1; —— : C1; —— : C1R1; in (b), color —— : Cold side; color —— : Hot side).

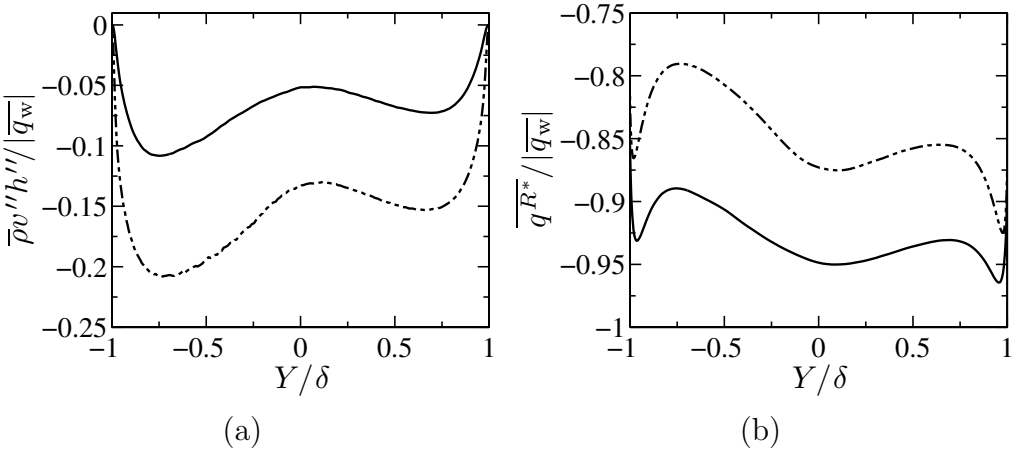

Figure 14: Comparison of turbulent convective heat flux (a) and radiative energy flux (b) of C4R1 and C1R1 (—··— : C4R1; —— : C1R1).

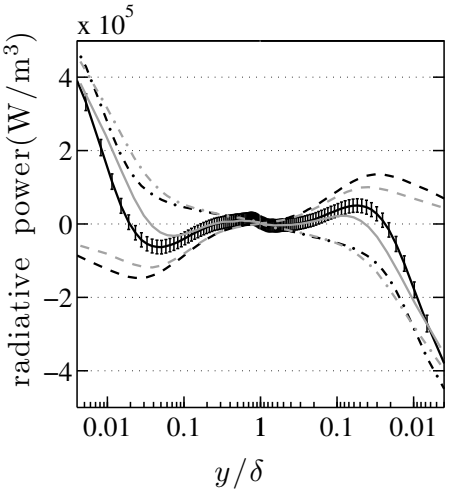

Figure 15: Mean radiative power profile of C4R1 and C1R1 on the cold (left) and hot (right) sides (—— : Total; – – : Gas-wall; – · – : Gas-gas; black lines : C4R1; gray lines : C1R1; the error bars represent the standard deviation).

perature profile and wall conductive flux, without undertaking a complete coupled computation. Such a computation has been achieved in this work, in typical combustion conditions, by coupling a direct numerical simulation of a turbulent channel flow with a radiative transfer model based on a Monte Carlo simulation, an optimized emission-based reciprocity and a CK or k gaseous radiative model.

When the radiative flux within a turbulent gaseous medium is of the same order of magnitude or higher than the averaged turbulent convective flux, or the wall conductive flux, strong coupling effects occur within all the medium and at the walls. It was shown that the usual temperature profile and its corresponding log-law are generally no more valid within a turbulent boundary layer. The couplings between conduction, turbulent convection and radiation are complex and first strongly depend on both gas-gas and gas-wall radiative interactions. The global radiation effects are not easily predictable as gas-gas and gas-wall radiative interactions bring contributions of opposite sign to the wall conductive flux. Moreover, depending on the transversal optical thickness of the gaseous medium, complex effects, that are linked to multiple wall reflections, can also occur and strongly modify both the averaged temperature profiles and the conductive wall fluxes. Finally, the averaged temperature profiles and wall conductive fluxes were shown to

also strongly depend on: i) the wall emissivities, that rule the wall reflection effects; ii) the temperature level, that controls the non linear radiative fluxes; iii) the Reynolds number that controls the weight of turbulence transport and the balance of gas-gas and gas-wall radiative effects.

The development of simpler models for the determination of the temperature profile in the turbulent boundary layer is necessary.

6. Acknowledgements

The first author is supported by a doctoral fellowship from China Scholarship Council (CSC). This work was granted access to the HPC resources of [CCRT/CINES/IDRIS] under the allocation 2012- 2b0164 made by GENCI (Grand Equipement National de Calcul Intensif). We also acknowledge Dr. Vincent Moureau and the SUCCESS scientific group for providing the code YALES2 and support.

7. Reference

[1] J. P. Gore, S.-M. Jeng, G. M. Faeth, Spectral and total radiation properties of turbulent carbon monoxide/air diffusion flames, AIAA J. 25 (1987) 339–345.

[2] J. Ji, Y. R. Sivathanu, J. P. Gore, Thermal radiation properties of turbulent lean premixed methane air flames, Proc. Combust. Inst. 28 (2000) 391–398.

[3] Y. Zheng, J. P. Gore, Measurements and inverse calculations of spectral radiation intensities of a turbulent ethylene/air jet flame, Proc. Combust. Inst. 30 (2005) 727–734.

[4] S. P. Burns, Turbulence radiation interaction modeling in hydrocarbon pool fire simulations, Technical Report SAND99-3190, Sandia National Labs., Albuquerque, NM (US); Sandia National Labs., Livermore, CA (US), 1999.

[5] H. R. Baum, W. E. Mell, Radiation and velocity fields induced by localized temperature fluctuations, Proc. Combust. Inst. 28 (2000) 473–479.

[6] A. Soufiani, P. Mignon, J. Taine, Radiation effects on turbulent heat transfer in channel flows of infrared active gases, in: Proceedings of the 1990 AIAA/ ASME thermophysics and heat transfer conference, HTD-137, ASME, pp. 141–148.

[7] Y. Wu, D. Haworth, M. Modest, B. Cuenot, Direct numerical simulation of turbulence/radiation interaction in premixed combustion systems, Proc. Combust. Inst. 30 (2005) 639 – 646.

[8] K. V. Deshmukh, D. C. Haworth, M. F. Modest, Direct numerical simulation of turbulence–radiation interactions in homogeneous nonpremixed combustion systems, Proc. Combust. Inst. 31 (2007) 1641–1648.

[9] K. V. Deshmukh, M. F. Modest, D. C. Haworth, Direct numerical simulation of turbulence–radiation interactions in a statistically one-dimensional nonpremixed system, J. Quant. Spectrosc. Radiative Transfer 109 (2008) 2391–2400.

[10] R. G. dos Santos, M. Lecanu, S. Ducruix, O. Gicquel, E. Iacona, D. Veynante, Coupled large eddy simulations of turbulent combustion and radiative heat transfer, Combust. Flame 152 (2008) 387 – 400.

[11] P. J. Coelho, Numerical simulation of the interaction between turbulence and radiation in reactive flows, Prog. Energ. Combust. 33 (2007) 311–383.

[12] P. J. Coelho, Turbulence radiation interaction: From theory to application in numerical simulations, ASME Conference Proceedings 2010 (2010) 251–270.

[13] S.-M. Jeng, G. M. Faeth, Radiative heat fluxes near turbulent buoyant methane diffusion flames, J. Heat Transfer 106 (1984) 886–888.

[14] P. J. Coelho, Detailed numerical simulation of radiative transfer in a nonluminous turbulent jet diffusion flame, Combust. Flame 136 (2004) 481–492.

[15] L. Tessé, F. Dupoirieux, J. Taine, Monte Carlo modeling of radiative transfer in a turbulent sooty flame, Int J. Heat Mass Transfer 47 (2004) 555 – 572.

[16] G. Li, M. Modest, Importance of turbulence radiation interactions in turbulent diffusion jet flames, J. Heat Trans.-T. ASME 125 (2003) 831–838.

[17] A. Gupta, M. F. Modest, D. C. Haworth, Large-Eddy Simulation of Turbulence-Radiation Interactions in a Turbulent Planar Channel Flow, J. Heat Trans.-T. ASME 131 (2009).

[18] S. Ghosh, R. Friedrich, M. Pfitzner, C. Stemmer, B. Cuenot, M. El Hafi, Effects of radiative heat transfer on the structure of turbulent supersonic channel flow, J. Fluid Mech. 677 (2011) 417–444.

[19] P. Damien, A. Jorge, E. H. Mouna, C. Benedicte, Analysis of the interaction between turbulent combustion and thermal radiation using unsteady coupled LES/DOM simulations, Combust. Flame 159 (2012) 1605–1618.

[20] R. S. Barlow, A. N. Karpetis, J. H. Frank, J. Y. Chen, Scalar profiles and no formation in laminar opposed-flow partially premixed methane/air flames, Combust. Flame 127 (2001) 2102–2118.

[21] A. Soufiani, Temperature turbulence spectrum for high-temperature radiating gases, J. Thermophys. Heat Tr. 5 (1991) 489–494.

[22] J. Amaya, O. Cabrit, D. Poitou, B. Cuenot, M. El Hafi, Unsteady coupling of Navier-Stokes and radiative heat transfer solvers applied to an anisothermal multicomponent turbulent channel flow, J. Quant. Spectrosc. Radiative Transfer 111 (2010) 295–301.

[23] A. Soufiani, J. Taine, Application of statistical narrow-band model to coupled radiation and convection at high temperature, Int J. Heat Mass Transfer 30 (1987) 437 – 447.

[24] H. Foysi, S. Sarkar, R. Friedrich, Compressibility effects and turbulence scalings in supersonic channel flow, J. Fluid Mech. 509 (2004) 207–216.

[25] P. Huang, G. Coleman, P. Bradshaw, Compressible turbulent channel flows: DNS results and modelling, J. Fluid Mech. 305 (1995) 185–218.

[26] G. Coleman, J. Kim, R. Moser, A numerical study of turbulent supersonic isothermal-wall channel flow, J. Fluid Mech. 305 (1995) 159–183.

[27] B. A. Kader, Temperature and concentration profiles in fully turbulent boundary layers, Int J. Heat Mass Transfer 24 (1981) 1541–1544.

[28] H. Kawamura, K. Ohsaka, H. Abe, K. Yamamoto, DNS of turbulent heat transfer in channel flow with low to medium-high Prandtl number fluid, Int. J. Heat Fluid Fl. 19 (1998) 482–491.

[29] P. Huang, P. Bradshaw, P, Law of the wall for turbulent flows in pressure gradients, AIAA Journal 33 (1995) 624–632.

[30] T. Nickels, Inner scaling for wall-bounded flows subject to large pressure gradients, J. Fluid Mech. 521 (2004) 217–239.

[31] O. Cabrit, F. Nicoud, Direct simulations for wall modeling of multicomponent reacting compressible turbulent flows, Phys. Fluids 21 (2009).

[32] J. Zhang, O. Gicquel, D. Veynante, J. Taine, Monte Carlo method of radiative transfer applied to a turbulent flame modeling with LES, Compt. Rendus. Mec. 337 (2009) 539–549.

[33] A. Soufiani, J. Taine, High temperature gas radiative property parameters of statistical narrow-band model for H_2O, CO_2 and CO, and correlated-K model for H_2O and CO_2, Int J. Heat Mass Transfer 40 (1997) 987 – 991.

[34] V. Moureau, P. Domingo, L. Vervisch, Design of a massively parallel CFD code for complex geometries, Compt. Rendus. Mec. 339 (2011) 141–148.

[35] V. Moureau, P. Domingo, L. Vervisch, From Large-Eddy Simulation to Direct Numerical Simulation of a lean premixed swirl flame: Filtered laminar flame-PDF modeling, Combust. Flame 158 (2011) 1340–1357.

[36] M. Kraushaar, Application of the compressible and low-mach number approaches to large-eddy simulation of turbulent flows in aero-engines, Ph.D. thesis, CERFACS, Toulouse, France, 2011.

[37] J. Kim, P. Moin, R. Moser, Turbulence statistics in fully developed channel flow at low Reynolds number, J. Fluid Mech. 177 (1987) 133–166.

[38] J. Kim, P. Moin, Transport of passive scalars in a turbulent channel flow, in: Turbulent Shear Flows 6th, pp. 5–2.

[39] N. Kasagi, Y. Tomita, A. Kuroda, Direct numerical simulation of passive scalar field in a turbulent channel flow, J. Heat Transfer 114 (1992) 598–606.

[40] L. Tessé, F. Dupoirieux, B. Zamuner, J. Taine, Radiative transfer in real gases using reciprocal and forward monte carlo methods and a correlated-k approach, Int J. Heat Mass Transfer 45 (2002) 2797 – 2814.

[41] Y. F. Zhang, O. Gicquel, J. Taine, Optimized emission-based reciprocity monte carlo method to speed up computation in complex systems, Int J. Heat Mass Transfer 55 (2012) 8172–8177.

[42] R. J. Kee, G. Dixon-lewis, J. Warnatz, M. E. Coltrin, J. A. Miller, A Fortran Computer Code Package For The Evaluation Of Gas-Phase, Multicomponent Transport Properties, Technical Report SAND89-8009, Sandia National Laboratories, 1986.

[43] R. J. Kee, F. M. Rupley, J. A. Miller, CHEMKIN-II: A FORTRAN Chemical Kinetics Package for the Analysis of Gas-Phase Chemical Kinetics, Technical Report SAND89-8009, Sandia National Laboratories, 1989.